Mathematical Geology, Vol. 36, No. 5, July 2004 (© 2004)

Weathering: Toward a Fractal Quantifying[1]

Klaudia Oleschko,[2] Jean-Francois Parrot,[3] Gerardo Ronquillo,[4] Sergey Shoba,[5] Georges Stoops,[5] and Vera Marcelino[5]

Weathering occurs over a wide range of scales. To link features through these scales is a major challenge for interdisciplinary weathering studies. Fractal approach seems to be specially useful for this purpose. We introduce a multistep fractal weathering assessment scheme devoted to extract fractal weathering classifiers from texture analysis of the mineral's image. Our scheme enables to quantitatively estimate the global and local information about the geometry of the weathering pattern. This information is basic to develop geometrical indices of weathering, which can significantly enrich the common qualitative and semiquantitative weathering assessment schemes. To justify the fractal approach, a strong statistical self-similarity has been documented for both the weathering and fresh features of two common silica minerals: quartz and biogenic A-opal (phytolith) over four orders of length scales. The procedure is fast, drastically reduces thresholding bias, promises to be universal, it is valid for genetically different minerals and rock types, scale independent, and specially useful for monitoring the changes in the mineral's roughness during the alteration. Two of the proposed classifiers seem to be potentially useful for direct application in the field and be used by nonspecialist.

KEY WORDS: scale invariance, texture, roughness, thresholding, quartz, phytolith.

INTRODUCTION

Weathering has become a vital interdisciplinary issue due to the general concern about its influence on the CO_2 budget, climate change (Benedetti and others, 2003; Lenton, 2001; Meunier, Colin, and Alarcon, 1999; Moulton and Berner, 1998; Strand, Passchier, and Näsi, 2003), and its effect on strength anisotropy of earth materials (Matsukura, Hashizume, and Oguchi, 2002). Its assessment has remained confused (Geol. Soc. Eng. Group Working Party Report, 1995), and

[1]Received 11 October 2002; accepted 9 March 2004.

[2]Laboratorio de Análisis Fractal de los Sistemas Naturales, Instituto de Geología, Universidad Autónoma de México, 04510 México, C.P., México; e-mail: olechko@servidor.unam.mx

[3]Instituto de Geografía, UNAM, 04510 México, C.P., México; e-mail: jfparrot@hotmail.com

[4]Instituto Mexicano del Petróleo, Eje Central 152, México, D.F., México; e-mail: gronqui@imp.mx

[5]Department of Geology and Soil Science, Gent University, Belgium; e-mail: georges.stoops@ugent.be

open to misinterpretation when classifying rocks and minerals by means of light and petrographic microscopy (Bourman and Ollier, 2002; Ehlen, 2002; Rivas and others, 2003). Several mineral- and rock weathering assessment schemes were introduced by three research communities—those looking for spectral attributes of weathering features (Delvigne, 1994, 1998; Ehlen, 1999; Marcelino and Stoops, 1996; Read, Kemp, and Rose, 1996); those quantitatively estimating mass loss (Duzgoren-Aydin, Aydin, and Malpas, 2002; Koptsik and others, 1999; Price and Velbel, 2003; Stutter, Smart, and Cresser, 2002; White and others, 1998); and those correlating alteration with petrographic and engineering index properties (Gupta and Rao, 2001). Notwithstanding, the geometry of weathering patterns and its relation to the mineral spectral attributes and mass loss still remains poorly studied. Over thirty chemical weathering indices have been proposed in the recent past (Duzgoren-Aydin, Aydin, and Malpas, 2002; Price and Velbel, 2003), most of them strongly biased and none of them valid for genetically different mineral and rock types and sufficiently precise for engineering purposes (Gupta and Rao, 2001). The use of most of these indices requires a high level of technical preparation.

In this study we propose four new fractal weathering classifiers to extract and measure the detailed geometrical features of the weathering pattern on multiscale digital images. Two of them are extracted by a simple, fully automatic procedure, which may be applied by anybody, independently of their expertise and the nature of the image. We propose to use these classifiers as the base to develop the general geometrical index of weathering, enabling to characterize both the topology of the system (the interconnectedness of individual elements) and its geometry (shape and size of the individual elements and their distribution), that is (Balankin, 1997), determine its morphology.

Fractal methods have become part of the standard approach to quantify the morphology (Heicht, 2000), spectral properties, orientation, connectivity, and tortuosity of weathering networks, pore–rock interfaces, and cracks (Brown, 1987; Krohn, 1988; Radlinski and others, 1999; Wong, Fredrich, and Gwanmesia, 1989). Weathering rates are adjusted well to a power function (White and Brantley, 2003). However, three main problems limit the general applicability of fractal based methods to image analysis: (1) The commonly used imaging procedures do not always preserve the self-similarity of fractal shapes; (2) Subjective, operator-dependent choices are made whenever fractal dimensions are computed from digitised images (thresholding); and, (3) An object can only be considered as fractal by ensuring its scaling behavior over a broad range of length scales. The classification procedure, which we designed, overcomes these three problems, and separates the local weathering information, from the global one.

To illustrate the new approach, we shall present a case history where all mentioned parameters are estimated with these new techniques. For calibration, we used two silica minerals: quartz and biogenic A-opal.

IMAGE FRACTAL ANALYSIS

Fractals are geometrical constructions with a number of specific properties (Mandelbrot, 1983). Fractal objects are complex both in their inhomogeneous texture and their outside roughness (Smith, Lange, and Marks, 1996). The lacunarity $\Lambda(r)$ and mass fractal dimension D_{M} measure the former, while the surface fractal dimension D_{S} the latter. Most of the measurable properties of fractal objects change as a noninteger power of scale. Self-similarity is the most striking property of isotropic fractals, where each piece of a shape is geometrically similar to the whole (physical self-similarity), and its statistical moments are the same upon resampling (statistical self-similarity) (Mandelbrot, 1983; Turner, Blackledge, and Andrews, 1998). The extent to which a self-similar fractal is translation-invariant is measured by its lacunarity. Self-affinity is another basic fractal concept, especially useful when dealing with rough surfaces, traces, or profiles. For self-affine objects the different geometrical directions should be scaled differently in order to preserve the shape or the statistical moments (Carr, 1997). Under the transformation $x \to \lambda_x x$ and $y \to \lambda_y y$, for a scale-invariant self-affine curve, the function $Y(\lambda_x x)$ satisfies the equation

$$Y(\lambda_{xx}) = \lambda_y Y(x) \cong \lambda_x^H Y(x),$$

where $H = (\ln \lambda_y)/(\ln \lambda_x)$ is called the roughness exponent or Hurst exponent (Meakin, 1993). The metric properties of a self-affine curve are characterized by the box-counting dimension $D_{\mathrm{box}} = 2 - H$ (Balankin, 1997).

If a self-similar or self-affine fractal form and the measure of its complexity are known at one resolution, it is possible to extrapolate the object's properties to any other scale, within the limits where it is fractal. In practice, a real system will only be fractal over some limited range of scales.

Fractal Imaging and Thresholding

When constructing an image of real world objects, the spatial and spectral information are combined through optical laws (Kolibal and Monde, 1998). Imaging a fractal means placing its spectral attributes, such as color, brightness, etc. in the 2-dimensional Euclidean space (Chen, Daponte, and Fox, 1989). The image may be divided into regions containing either deterministic information (well handled by Euclidean geometry, and extractable by edge detection) or textural information (described by fractal geometry). We show how to combine both kinds of information inside the geometrical weathering classification based on the detailed quantitative estimation of the altered and fresh features.

From the perspective of image processing, texture is defined as spatial variation in grey tones, arising from the changing patterns of brightness and darkness through the image (Turner, Blackledge, and Andrews, 1998). This study applies fractal approach to texture analysis in order to: (1) Measure roughness and lacunarity of grey tone distribution across the mineral surface, and its change with weathering; (2) Establish a possibly less biased threshold between the spectral attributes of weathering features and fresh solid matrix; and (3) Measure and compare the most common fractal parameters of weathering and fresh features.

MATERIALS AND METHODS

The semiquantitative weathering scheme (Marcelino, Mussche, and Stoops, 1999) that reflects increasing degree of quartz weathering on the basis of etch pits frequency and size was used for initial classification of the quartz and the long cell morphotype of phytoliths. Four contrasting classes of weathering were compared for studied grains: (1) Fresh (Class A); (2) Slightly weathered (Class B); (3) Weathered (Class C); and, (4) Highly weathered (Class D).

The analysis of each mineral was limited to one size fraction. The medium sand (250–500 μm) quartz grains were selected from the Luvic Acrisol, (Tabasco State, Mexico) a highly acid tropical soil with pH = 4 (Fig. 1).

Phytoliths (20–50 μm) were concentrated by gravity sedimentation from the humus horizon of Ochric Andosol of Nevado de Toluca (Mexico). The opal-phytoliths exhibit distinct features of alteration—dissolution (Benayas Casares, 1963) or microcavities (Alexandre and others, 1997), resulting in characteristically corroded forms (Fig. 2).

Most weathering features occur over a wide range of scales from microns to meters. To analyze the scaling of quartz features, combined optical (from $\times$ 2.5-upper cutoff to 40) and scanning electron microscope (from $\times$ 50 to 20000-lower cutoff) photomicrographs were used, covering 10 different magnifications. For phytoliths only electron microscope grey scale images (magnification from $\times$ 850-upper cutoff to 10000-lower cutoff) were utilized.

The fractal analyses of optical and SEM images were accomplished using the BENOIT program package (BENOIT 1.2) recommended as the reference software (Seffens, 1999). BENOIT contains five self-similar and five self-affine techniques. For the self-similar images, the program acts upon two-dimensional bitmap version, while the self-affine methods require a linear array of data. We show how to combine both techniques in order to make precise the weathering advance estimation. For the lacunarity measurement, our own program was used (Oleschko and others, 2004).

It is well known that several fractal dimensions are required for the complete description of a fractal, each one having special significance and useful for

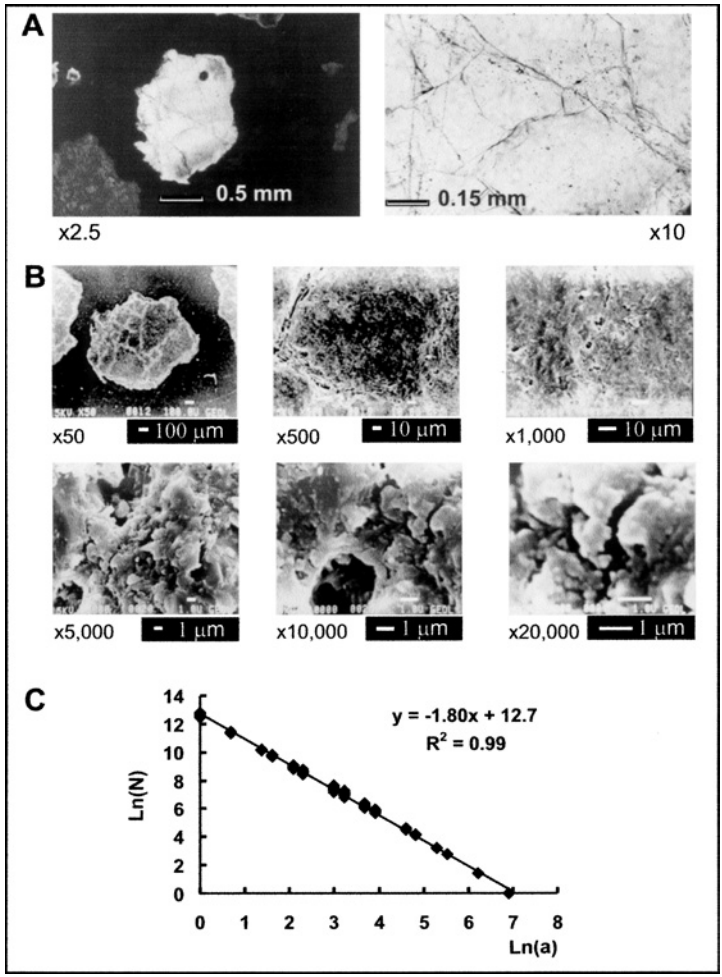

Figure 1. Plane polarized light (A) and backscattered electron (B) micrographs of a weathered quartz grain. (C): Self-similarity of the weathering features observed at different magnifications. Ten sets of points, resulting from the box counting analysis of weathering features extracted from ten images, with resolution from 2.5 to 20,000, analyzed all together in plot (C) (a is box size in microns, $N = N(a)$ number of a-sized boxes covering the weathering pattern).

particular attribute measurements. The box counting (D_{box}) and rescaled range ($D_{\text{R/S}}$) fractal dimensions have been found the most appropriate for the following discussion, and proved to be robust for the weathering assessment.

All fractal parameters extracted from the experimental grains were compared with D_{box}, $D_{\text{R/S}}$, and lacunarity measured on the reference images of Marcelino

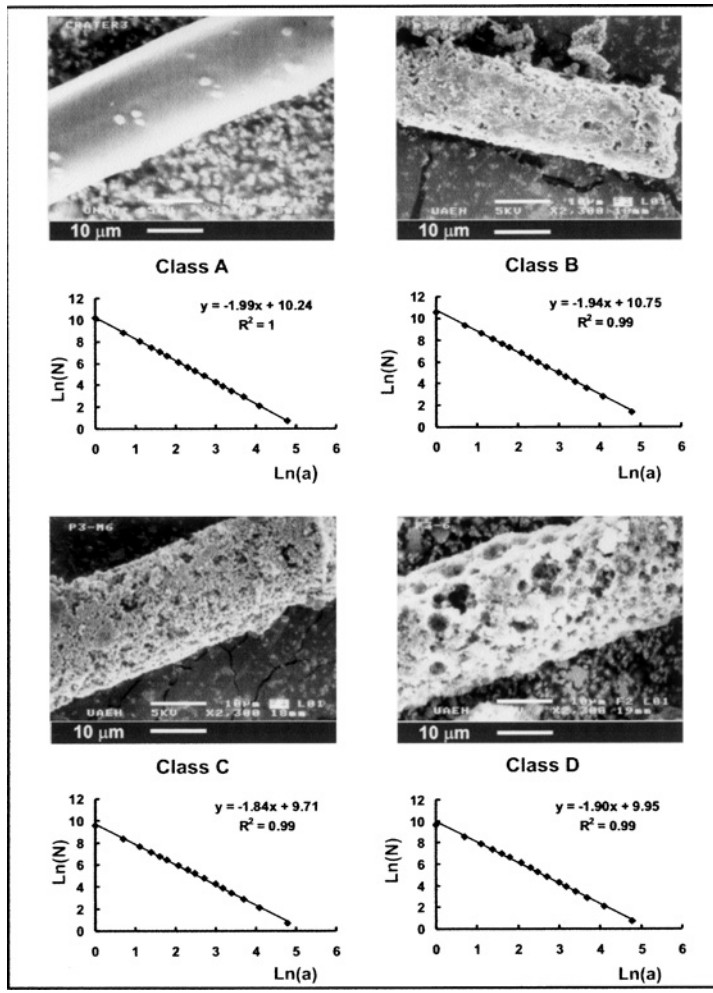

Figure 2. Backscattered electron micrographs of four phytoliths with increasing degree of weathering, from fresh (Class A) to highly weathered (Class D), and box-counting analyses of the respective solid surfaces. The decrease in fractal dimension of solids (the slope of the graphs) with weathering advance is indicator of the mineral alteration.

and Stoops (1996), used for the initial semiquantitative grains weathering classification, based on the morphology of the alteration features.

First of all, a statistical analysis of the data bank, was accomplished using all data independently of image origin. For this purpose, and in order to have the same grey tones for the pores and solids, all SEM images, previously to the fractal

analysis, were converted to their negatives, prior to fractal analysis. Then, the same analysis was applied to the quartz, phytoliths, and reference images separately from each other. Finally the detected statistical tendencies were confirmed comparing the images of the same nature (optical images were analyzed separately from the SEM, experimental grains separately from the reference ones, etc.), resolution (comparing the images of four weathering classes for the same magnification), and maintaining the similar size of images.

SELF-SIMILARITY OF THE WEATHERING PATTERNS AND FRACTAL CLASSIFIERS

The first point to verify in this research has been the self-similar nature of weathering—and fresh features of quartz and phytoliths over the compared four orders of magnitude length scales. Starting out from the mineral, optical, and SEM grey scale images, we documented a strong statistical self-similarity for both mentioned features, for quartz and phytoliths as well, which may be observed on analysis not only on the original images (Figs. 1 and 2), but also imprinted in the firmagrams (Fig. 3). In the latter case, strong self-affinity was detected for the whole sequence $F(x, y)$ of grey tones obtained by transforming the image into a linear array of values following line by line the spatial order of pixels. This sequence has been shown to be a self-affine fractal function, with rougness close to the original image. Therefore, both the optical and SEM images preserve the self-similarity of the weathering and fresh patterns. From the obtained results, we derived four weathering classifiers: mineral weathering signature or *firmagram* (C1); generalized lacunarity (C2); heterogeneity of the weathering—and fresh features distribution across the grain surface (C3); continuity and tortuosity of the solid and pore patterns (C4). The first two classifiers (C1 and C2), do not require any image segmentation prior to fractal analysis, and may be directly applied to the mineral or rock image in the laboratory or in the field. The other two classifiers (C3 and C4) can be used only for the thresholded images, segmented into the weathering and fresh features. For the latter purpose, we designed an edge detection technique, called Local Fractal Analysis.

Mineral Weathering Signature or Firmagram (C1)

The $N \times N$-sized image (.raw extension) is converted by our technique to a linear array of grey tone values following the spatial order of pixels line by line. The array starts with pixels of the first line from coordinates (1, 1) to (1, N), followed by pixels of the second line from (2, 1) to (2, N), etc. An image with 200×200 pixels is represented by 40,000 data. This grey-scale sequence $F(x, y)$ is a self-affine

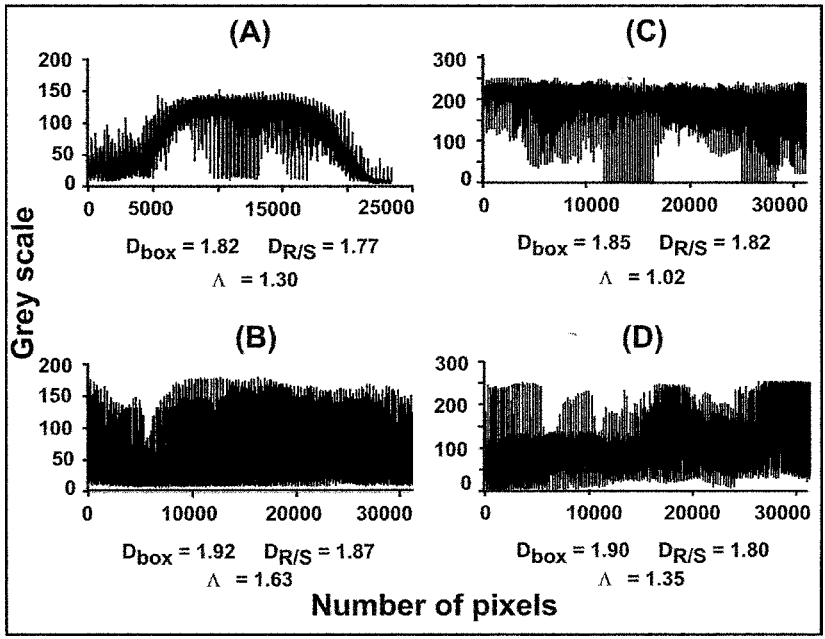

Figure 3. Quartz and biolith weathering signatures shown as compressed graphs, called "firmagrams," of whole-image grey-tone distributions. Compare the fresh (biolith-(A) and quartz-(C)), and highly weathered ((B) and (D), respectively) grains. The visually appreciable changes in the firmagrams correlate well with the advance in mineral weathering, and may be quantified by box counting (D_{box}) and rescaled-range ($D_{\text{R/S}}$) fractal dimensions. Both mentioned dimensions show the increase of roughness, coinciding with the bigger lacunarity in highly weathered minerals.

fractal function. We proved mathematically (Oleschko and others, 2004), that if it is self-affine fractal with roughness exponent α (Barabasi and Stanley, 1995), that is if $\text{Var}(\xi) = \langle [F(x, y) - F(x + x', y + y')]^2 \rangle \propto \xi^{\alpha}$ for $\sqrt{x'^2 + y'^2} \leq \xi$, then the variance of the sequence $f_1 = p(1, 1), \ldots, f_{N^2} = p(N, N)$ also scales with the same exponent:

$$\text{Var}(k) := \langle [f_i - \langle f_i \rangle]^2 \rangle_{i \in \{1,\ldots,N^2\}}$$

$$= \left\langle \frac{1}{k} \sum_{j=i}^{i+k} \left[f_j - \frac{1}{k} \sum_{l=i}^{i+k} f_l \right]^2 \right\rangle_{i \in \{1,\ldots,N^2\}} \propto k^{\alpha} \left(1 + O\left(\frac{k}{N} \right) \right).$$

This self-affine sequence can be analyzed by any reference technique available to estimate the fractal parameters of self-affine curves. In the present discussion we

refer only to the rescaled-range fractal dimension ($D_{R/S}$), measured by BENOIT program package.

The compressed graph of this self-affine sequence, extracted from the image and termed by us *firmagram*, visualizes the entire data density distribution (Oleschko and others, 2004), and is specially useful for a first qualitative estimation of the degree of mineral alteration. The fractal behavior of this density distribution can be characterized by D_{box}, applying box counting directly to the firmagram, viewed as a 2-dimensional image (Fig. 3) or by the rescaled-range fractal dimension calculated for the whole grey tone distribution. For all analyzed grains these two dimension values were very close. Two pairs of contrasting firmagrams for fresh (Class A) and highly weathered (Class D) quartz and phytolites are shown in Figure 3. The firmagram's D_{box} fluctuated between 1.85 (Class A), and 1.90 (Class D) for quartz (Fig. 3(C) and (D)), and between1.82 (Class A) and 1.92 (Class D) for phytoliths (Fig. 3(A) and (B)). Sometimes the variation of the fractal dimension and Hurst exponent values looks small, or is not observed (for instance $D_{R/S}$ of quartz, Fig. 3(C) and (D)). In this case, the major precision may be achieved at the second step of analysis (see *reference lines*, Fig. 4), or taking into account the dynamics of the other fractal parameter (see lacunarity). However, it should to be taken into account that both mentioned parameters are exponents of power laws, so that high porosity variation can arise from small D_{box} and $D_{R/S}$ changes. Thus, our results show that the fractal dimension as well as the Hurst exponent are sufficiently sensitive parameters for quantifying weathering degrees. We conclude that the firmagram encodes the global spatial information about the mineral density in a synthetic form which can be easily obtained by fractal analysis both qualitatively and quantitatively.

The firmagram, proposed by us as global fractal signature of the image's grey tone distribution, contains global quantifiable information about the mineral surface roughness. The grey tone distribution yields an exact profile of the image, showing all changes in pore density occurring across the mineral's surface with the precision of one pixel. This enables the researcher to select areas (or profiles) of specific interest and to extract and measure *reference lines*, obtaining the local weathering information. Figure 4 shows the examples of reference lines with corresponding fractal parameters, for contrasting weathering classes of quartz (Fig. 4((D)–(F))) and phytoliths (Fig. 4((A)–(C))). For comparison, all reference lines were extracted from the center of corresponding image. However, any reference line corresponding to any selected part of the image, and containing measurable information about the weathering, can be selected for analysis. The clear visual differences observed in roughness and lacunarity between fresh and highly weathered grains are proved to be statistically significant (Fig. 5). The fractal parameters extracted from the complete firmagram and from randomly selected reference lines for four compared weathering classes of quartz and phytoliths (from A to D), show clearly and independently of mineral genesis or the

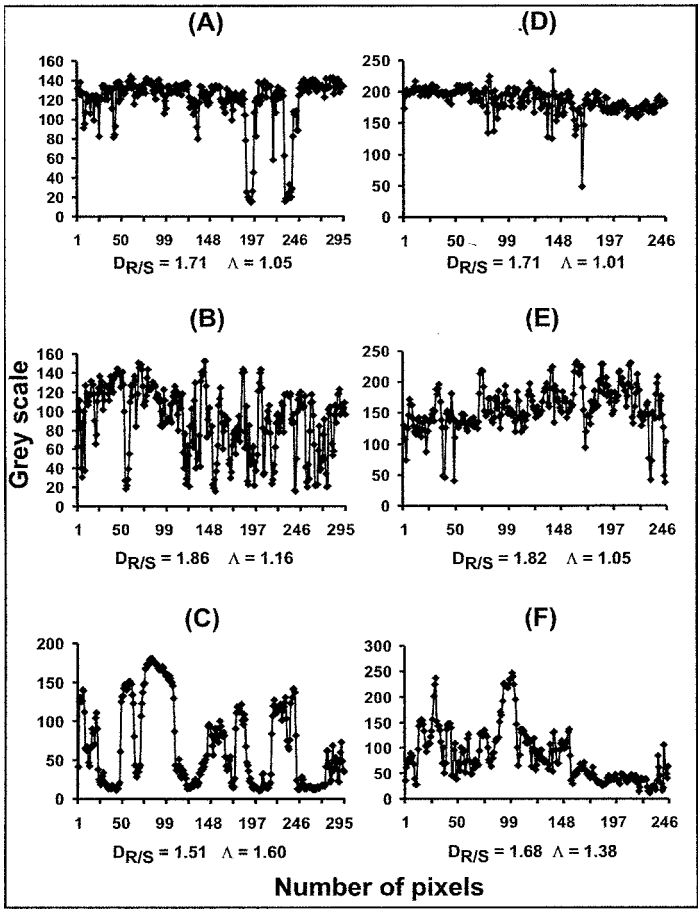

Figure 4. Six reference lines, extracted from the center of the corresponding images, and their respective fractal parameters, for contrasting weathering classes (Class A: (A) and (D); Class B: (B) and (E); Class D: (C) and (F)) of phytoliths ((A)–(C)) and quartz ((D)–(F)). The grey tone distribution across the reference lines shows the changes in pore number and size with the precision of 1 pixel. The local dynamics occurred in the geometry of weathering pattern, measured by fractal parameters, coinciding with the global tendencies in Figure 3: the surface roughness and lacunarity increase with weathering advance.

origin and magnification of the image, the increase of roughness with weathering advance. The statistically significant decrease of the Hurst exponent (and corresponding increase of D_{box} and $D_{R/S}$) during alteration is attributed to an increase in roughness of the mineral's surface. This tendency is better described by hyperbolic relation ($R^2 \approx 0.6$, Fig. 5(A)), whose adjustment can be further improved

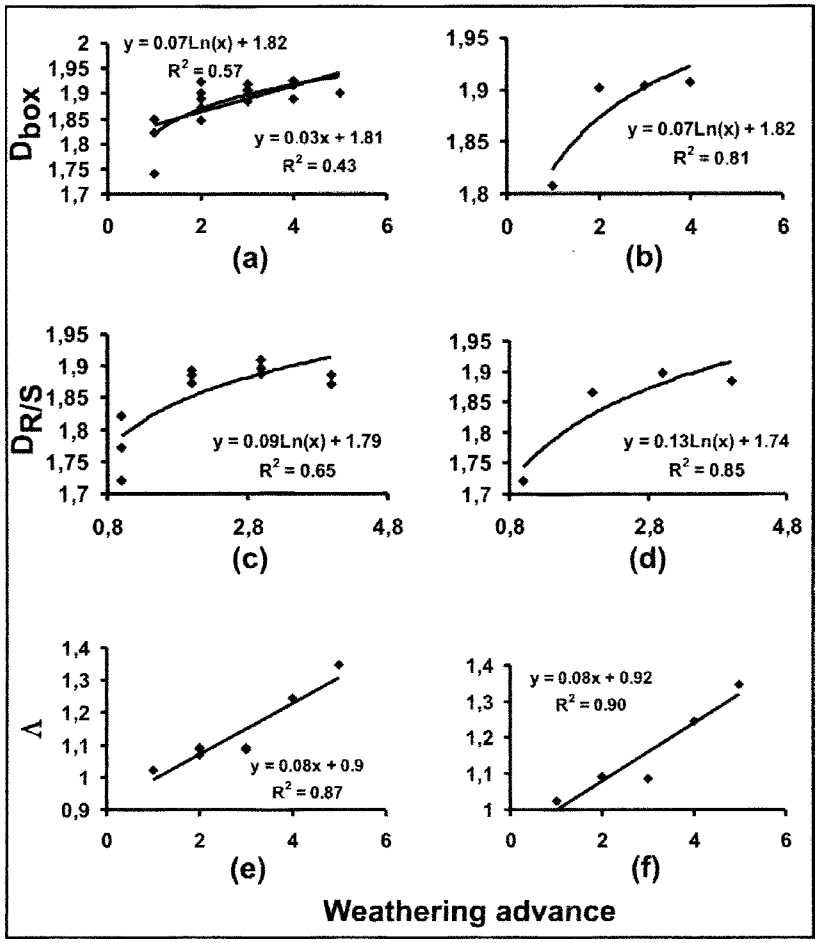

Figure 5. Results of statistical analyses applied to all images, (A), (C), and (E), compared with indivudual grain statistics (B), (D), and (F). The clear hyperbolic increase in image roughness with weathering is measurable in terms of box-counting (D_{box}: (A) and (B)) and rescaled-range ($D_{R/S}$: (C) and (D)) fractal dimensions. A statistically significant growth of lacunarity with alteration ((E) and (F)) is observed in all analyzed images.

(to $R^2 \approx 0.8$, Fig. 5(B)) if the data are analyzed grain by grain. In general terms, we concluded that the roughness of the image is suddenly increased in quartz and phytolith images from Class A (H = 0.29–0.29) to Classes B (H = 0.18–0.14) respectively, and then clearly fell down (Class D, H = 0.32–0.49). The same H, D_{box}, and $D_{R/S}$ dynamics was observed for the reference images of quartz (Marcelino, Mussche, and Stoops, 1999; Marcelino and Stoops, 1996).

Generalized Lacunarity (C2)

Mandelbrot (1983) called a fractal "lacunar" if it had arbitrarily large gaps. Plotnick and others (1996) have extended the lacunarity concept to characterize the spatial distribution of geological data. In this study we generalized the approach of Allain and Cloitre (1991) and introduced a variable $\Lambda(r)$, where r is scale, to measure the spatial variation of grey tones across the mineral surface. $\Lambda(r)$, called "generalized lacunarity," measures the extent to which an image or map is not translationally invariant. $\Lambda(r) = 1$ for a completely filled black or white square, and in the general case it is calculated as the ratio of the mean-square $[Z_Q^2(r)]$ of the fluctuations in grey tone distribution to their squared mean $[Z_Q(r)]^2$:

$$\Lambda(r) = \frac{Z_Q^2(r)}{[Z_Q(r)]^2}.$$

The generalized lacunarity, for $r = 1$ (which is the size of a single pixel), is used as the second weathering classifier (C2). The mean value of $\Lambda(r)$ estimated on the firmagram (global level) was close to 1 in fresh quartz (1.02), bigger in fresh phytolith (1.30), increasing to 1.35 and 1.63, respectively in highly weathered grains (Class D). The mean lacunarity extracted from the reference lines is changed from 1.01 (Class A), to 1.05 (Class B) and 1.38 (Class D) for quartz, and from 1.05, to 1.16 and 1.60 for phytolits, respectively. A clear influence of mineral genesis has thus been documented for the lacunarity dynamics under alteration. From the beginning of weathering, lacunarity analysis enables to detect statistically significant ($R^2 = 0.87$, Fig. 5(E)) differences in the pores' distribution, and homogeneity between minerals of contrasting genesis, including biogenic silica accumulation.

Edge Detection: Local Fractal Analysis (LFA)

The fractal dimension assumes a black and white, binary world-view, where a specific point is either a member of the fractal or not (Voss and Wyatt, 1993). Several thresholding algorithms are available to generate binary images whenever fractal image dimensions are evaluated (Baveye and others, 1998). In the present study, prior to the fractal analysis, all original images were transformed to so-called measure images, applying Local Fractal Analysis (LFA, see Pentland, 1984). LFA also provides a global characterization of the image in terms of its local fractal dimension distribution (lfd). The analysis is performed locally on grey tone images, by calculating the local fractal dimension of each pixel inside sliding boxes.

Assume we have the grey tone image $I(i, j)$, where i and j are pixel coordinates, $I(i, j)$ is the grey tone value. With a properly selected integer, s, take a sliding box of size $s \times s \times s$. When the sliding box's center gets positioned at a given pixel, the volume cut out of the box by the grey tone surface will be measured in terms of voxels. A voxel is an elementary cube the sides of which are equal to pixel size, and the grey tone surface should be properly scaled by a factor h to be commensurate with cube size. Above a given pixel (i, j) the box contains a number $vs(i, j)$ of voxels, $0 \leq vs(i, j) \leq s$. The total number of voxels (Vs) in the whole box under the surface is, for an even-sized cube:

$$Vs = \sum_{k=-s/2}^{s/2} \sum_{l=-s/2}^{s/2} vs(i + k, j + l),$$

where $vs(i, j)$ is defined as:

$$vs(i, j) = \begin{cases} T(i, j) & \text{if} \quad 1 \leq T(i, j) \leq s \\ s, & \text{if} \quad T(i, j) \geq s \\ 0, & \text{if} \quad T(i, j) \leq 0 \end{cases},$$

with

$$T(i, j) \left(\frac{I(i, j) - Ic}{ps} \times h \right) + \frac{s}{2}. \tag{1}$$

Here $I(i, j)$ is the grey tone in the original image, Ic the grey-tone value of the central pixel, ps the pixel size, h a coefficient used to scale the surface altitude (see later), and s the cube's size.

In the next step the box is divided into smaller boxes of size a varying between 1 and $s/2$ (Fig. 6(I). Each of these boxes is considered as filled if it contains at least one voxel. Then, the maximum of $vs(i, j)/q$ involved in each cell is defined by the set of a values, the total number of filled boxes being:

$$Ns(a) = \sum_{i=1}^{s/a} \sum_{j=1}^{s/a} \underset{0 \leq m < a}{\text{Max}} \{Vs(i \times a - m, j \times a - m)\},$$

where Max is a function returning the maximum value.

On a double logarithmic plot $Ns(a)$ versus a appears as an approximately straight line, the inverse slope of which yields the local fractal dimension $Ds \in [0, 3]$.

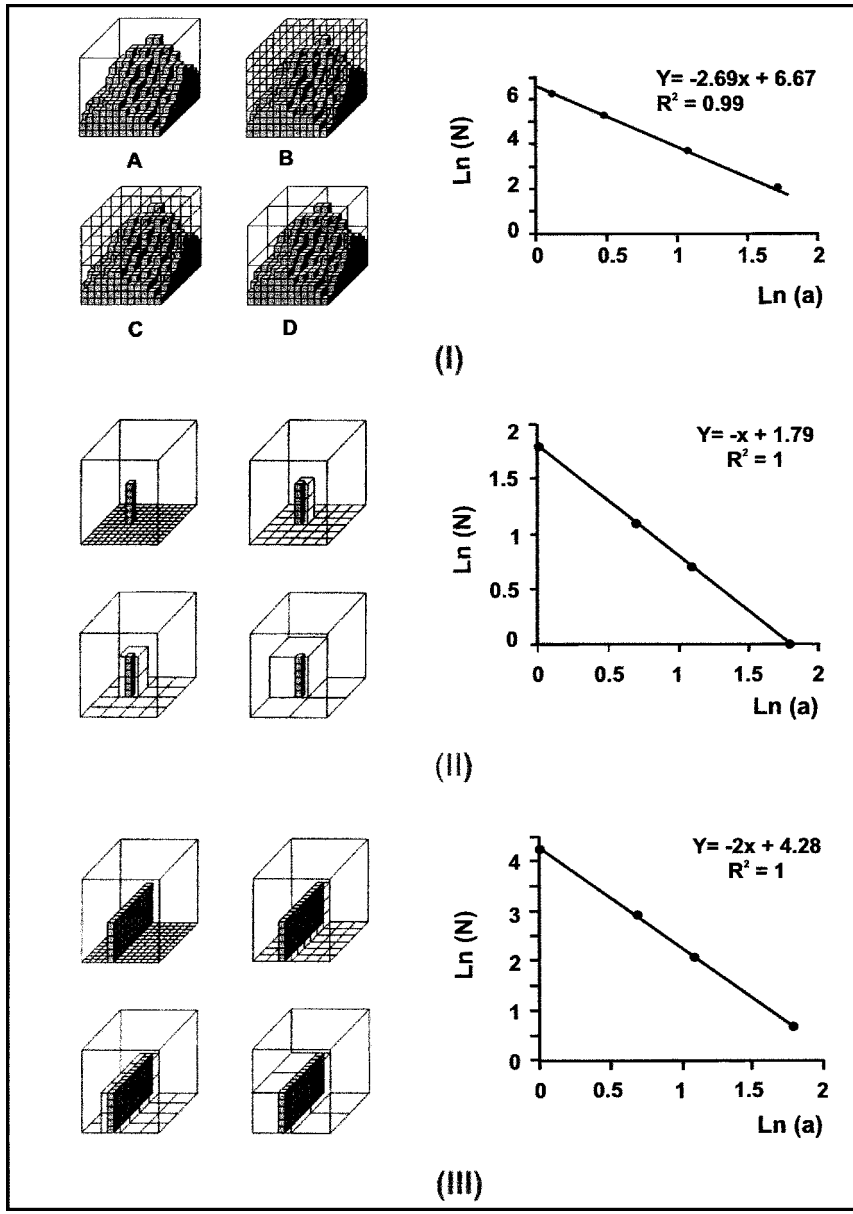

Figure 6. Examples of D_S calculating (I) inside a cube of size $12 \times 12 \times 12$ pixels with different divisors a: (A) $a = 1$; (B) $a = 6$; (C) $a = 4$; (D) $a = 2$. Local Fractal Analysis of a point (II) and a line (III) are shown too.

When calculating the slope, the squared coefficient of correlation R^2 is also computed. The estimated fractal dimension depends on the following factors.

Role of the Coefficient h

The grey tone and the spatial coordinates on the x, y-axis do not have the same unit of measurement. If the size of a pixel is considered equal to 1, by Equation (1), the volume inside the box depends on the h coefficient and on the grey level variation $I(i, j) - Ic$. High h values accentuate surface roughness, because the large weight of the first term makes it more important than the second one, $s/2$. On the contrary, low h values produce smooth surfaces, because the second term of the formula becomes predominant. Consequently, it is possible to adjust the value of h to the nature of the analyzed surface.

Size of the Sliding Window and Range of Grid Sizes

For LFA, it is possible to use different window sizes, for instance 12 or 24. Even-sized windows with many exact divisors (up to $s/2$) provide a regular slope. Sliding windows with odd size lead to a slight deviation from the theoretical slope because none of the exact divisors, defining the set of grid sizes q, would correspond to half of an odd window size.

In case of a $12 \times 12 \times 12$-size sliding cube (Fig. 6(I)) there are five exact divisors ($a = 1$, 2, 3, 4, and 6), in case of the $24 \times 24 \times 24$ box there are seven ($a = 1, 2, 3, 4, 6, 8$, and 12). Calibration on a point and a line, accomplished using these two cubes, resulted in the correct dimensions (1, 2 respectively) with $R^2 = 1$ in both cases (Fig. 6((II)–(III))).

In general, a smaller window accentuates small irregularities, whereas a greater one would emphasize the more general features of the image.

Definition of the Centre for an Even Window

As discussed above, the results are better for even-sized windows than for odd-sized ones. However, in the first case, it is necessary to define the concept of "centre," since the reference point of the algorithm cannot be exactly located in the true geometric center but only in one of the four points surrounding it. An arbitrary selection of any of these four points would lead to a slight bias. In this study we defined the value at the centre as the mean of the four pixels located around it.

The local fractal dimension D is not strictly a dimension, as it can take values outside the topological limits, like $D < 0$ or $D > 2$, for 2-dimensional images (Voss and Wyatt, 1993). The D value is linearly transformed to a grey

scale value, between 0 and 255 in such a way that in the transformed image white corresponds to high fractal dimensions ("rough") and black to low ones ("smooth"). The procedure is similar to the Digital Elevation Model (Luca, Datcu, and Seidel, 1996), because the grey tone is treated as altitude, and it results in a transformed image with clear edge enhancement along boundaries of weathering features (Fig. 7((D)–(F))). The reason why the local fractal dimension detects and enhances edges is that edges add a deterministic component to the surface, that is they decrease the local dimension (Toennies and Schnabel, 1994, Fig. 7(F)). Before fractal analyses a visual comparison is made between the original and the measure images: only when they look similar (Fig. 7((A)–(F))), is

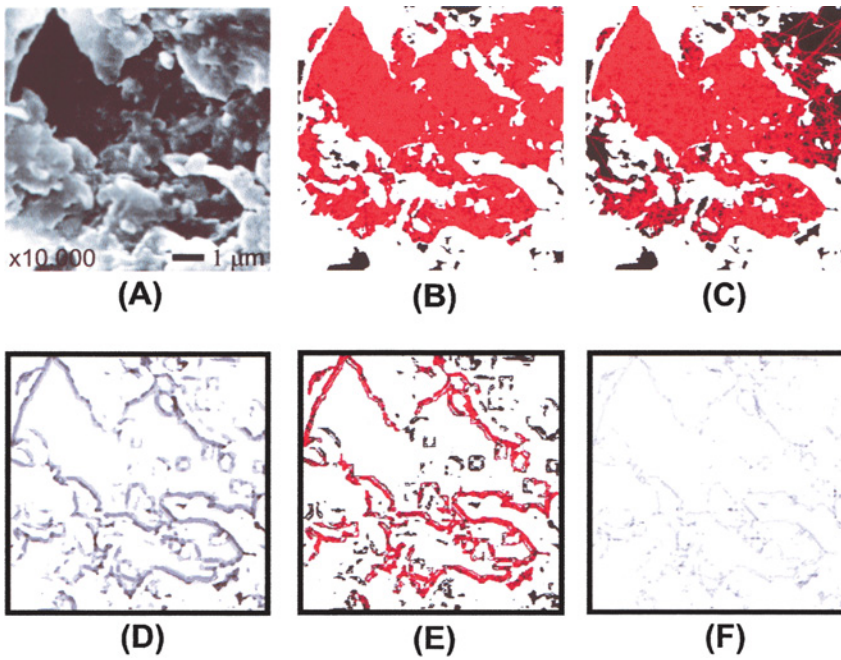

Figure 7. (A): Digital image of a quartz grain (SEM, × 10,000); (B): The measure image resulted from the continuous-time random walks algorithm, applied directly on (A) during thresholding by Brownian motion: The map is constructed using 1000 walks; (C) Same as (B), but obtained by 100 random walks: The measure image has lower precision; (D) The measure image produced by Local Fractal Analysis ($h = 0.01$): A transformed image shows clear edge enhancement along boundaries of weathering features; (E): Continuous-time random walks algorithm applied on measure image (D): The continuity of boundaries between pores and fresh matrix is measured by the spectral dimension; (F): Map of the coefficient of determination (R^2) calculated for each pixel during LFA. Note that boundaries have lower R^2 (darker color) due to their deterministic nature.

thresholding considered correct. The map of R^2 distribution across the analyzed image, resulted from the local fractal analysis for each pixel and transformed in greys (Fig. 7(F), looks similar to image with detected edges obtained by LFA (Fig. 7(D))).

Two groups of algorithms were applied to images after thresholding: BENOIT, a commercially available fractal analysis software for Windows (Seffens, 1999), and specially designed scientific programs (Parrot and Rico, 1997).

Heterogeneity of Weathering Features Distribution (C3)

The mass fractal dimension (D_M) measures the space-filling ability and heterogeneity of weathering—and fresh features distributions across the mineral surface. It is always less than 2, which is the topological limit for a completely filled rectangle. The solid set's fractal dimension was close to 1.99 both in the fresh quartz and in the phytolith (Class A), decreasing to 1.89 and 1.85, respectively, in highly weathered grains (Class D, Figs. 1 and 2). This change reflects the reduction of the solid mineral surface during weathering, visually observed as the increase in the density of black pixels inside the firmagram (Fig. 3). The black part of the fresh minerals firmagram always occupied the opposite position on the graphic in comparison with the highly weathered quartz and phytolith. Referring to the D_M this dynamics was interpreted as the pore dimension growth with alteration. A significant increase from 1.62 (Class A) to 1.84 (Class D), and from 1.40 (Class A) to 1.87 (Class D), was documented for pore pattern of both quartz and phytoliths, respectively. Inside the rest of the compared weathering classes, both minerals occupy intermediate positions in the values of solid and pore mass fractal dimensions.

Continuity and Tortuosity of the Patterns (C4)

Whereas the above discussed parameters measure static features, the spectral dimension $\bar{d}$ describes the dynamic properties of fractal networks (Alexander and Orbach, 1982). This parameter is defined in terms of the random walk of particles along paths constrained to the fractal set. Therefore $\bar{d}$ is a measure of network connectedness, related to its lacunarity. A larger spectral dimension indicates a more continuous, less tortuous pattern. The spectral dimension is estimated by constructing continuous-time random walks (CTRW's: Orbach, 1986), starting from a random pixel of the image with a given grey value, and continuing through pixels with the same grey tone. The map of the fractal dimensions of these walks is the other measure image, which should coincide with the original one if thresholding is correct (Fig. 7((B)–(C))). We found that $\bar{d}$ is a good discriminator of grain

weathering level, able to measure the connectedness of each specific weathering feature additionally to the global connectivity analysis. For instance, Figure 7(E) shows the measure image used for $\bar{d}$ calculation for the boundaries between the grain pores and matrix. Thus, both global and local measurements can be accomplished by this method too. In case of fresh quartz grains and phytoliths, the connectedness of the solid matrix was maximum, and $\bar{d}$ was largest (1.99), close to the D_{m} value and coincided with the maximum image translation invariance (lacunarity close to 1). The connectivity of the weathering features was so minimal that no random walks could be accomplished. In a highly weathered quartz, the spectral dimension of the solid set falls to 1.88, increasing to 1.79 for the pores, and coinciding with the high lacunarity which may be clearly observed on the reference line behavior. The connectivity was larger in the pore set of phytoliths, where $\bar{d}$ reaches 1.85 in Class D, and decreases to 1.82 for the solid set of the same weathering class, which confirmed once more the higher initial porosity of phytoliths in comparison with fresh quartz, detected by visual and quantitative lacunarity analyses.

CONCLUSIONS

We demonstrated that the grey tone distribution across the optical and SEM images can be used to derive simple and precise geometrical measures of weathering advance. Four objectively assessable fractal weathering classifiers were proposed to qualitatively and quantitatively discriminate between weathering and fresh features. The method is also efficient in the case of low scale ($\times 2.5$) images. Therefore the proposed multistep weathering assessment scheme is potentially useful for direct application to the first field estimation of the minerals' and rock degree of alteration. The proposed quantitative procedure correctly classified the weathering grade of quartz and phytolith grains, in agreement with the semiquantitative weathering scheme of Marcelino, Mussche, and Stoops (1999), regardless of scale. These results open up new vistas for a multiscale classification of mineral weathering and correlation of mineral morphology dynamics to the mass loss. The procedure seems to be valid for genetically different materials, and independent of the geomorphologic or environmental conditions.

ACKNOWLEDGMENTS

We want to thank Dr. G. Korvin for the manuscript revision and very helpful comments. We are also grateful to Dr. S. Sedov for phytoliths SEM imaging, and D. A. Hernández, A. González V., and M. Reyes S. for technical support. This research was supported by CONACYT (33099-A), PAPIT (UNAM, IN114000,

IN102802), ECOS program (México), and grant D2102 YNF Program of Instituto Mexicano del Pbvetroleo.

REFERENCES

Alexander, S., and Orbach, R., 1982, Density of states on fractals: <<fractons>>: J. Phys. Lett., v. 43, p. L625–L631.

Alexandre, A., Meunier, J.-D., Colin, F., and Koud, J.-M., 1997, Plant impact on the biogeochemical cycle of silicon and related weathering processes: Geochim. Cosmochim. Acta, v. 61, p. 677–682.

Allain, C., and Cloitre, M., 1991, Characterizing the lacunarity of random and deterministic fractal sets: Phys. Rev. A, v. 44, p. 3552–3558.

Balankin, A., 1997, Physics of fracture and mechanics of self-affine cracks: Eng. Fracture Mech., v. 57, p. 135–203.

Barabasi, A.-L., and Stanley, H. E., 1995, Fractal concepts in surface growth: Cambridge University Press, Cambridge, UK.

Baveye, P., Boast, C., Susumu, O., Parlange, J. I., and Steenhuis, T., 1998, Influence of image resolution and thresholding on the apparent mass fractal characteristics of preferential flow patterns in field soils: Water Resour. Res., v. 34, p. 2783–2796.

Benayas Casares, J., 1963, Partial solution of silica of organic origin in soils: Ann. Edafol. Agrobiol., v. 22, p. 623–626.

Benedetti, M. F., Dia, A., Riotte, J., Chabaux, F., Gérard, M., Boulégue, J., Fritz, B., Chauvel, C., Bulourde, M., Déruelle, B., and Ildefonse, P., 2003, Chemical weathering of basaltic lava flows undergoing extreme climatic conditions: The water geochemistry record: Chem. Geol., v. 201, p. 1–17.

Benoit 1.2, Trusoft International Inc. St. Petersburg, FL: http://www.trusoft-international.com

Bourman, R. P., and Ollier, C. D., 2002, A critique of the Schellmann definition and classification of "laterite": Catena, v. 47, p. 117–131.

Brown, S. R., 1987, A note on the description of surface roughness using fractal dimension: Geophys. Res. Lett., v. 14, p. 1095–1098.

Carr, J. R., 1997, Statistical self-affinity, fractal dimension, and geological interpretation: Eng. Geol., v. 48, p. 269–282.

Chen, C.-C., Daponte, J. S., and Fox, M. D., 1989, Fractal feature analysis and classification in medical imaging: IEEE Trans. Med. Imaging, v. 8, p. 133–142.

Delvigne, J., 1994, Proposals for classifying and describing secondary microstructures observed within completely weathered minerals, *in* Ringrose-Voase, A. S., and Humphreys, G. S., eds., Soil micromorphology: Studies in management and genesis: Elsevier, Amsterdam, p. 333–342.

Delvigne, J. E., 1998, Atlas of micromorphology of mineral alteration and weathering: The Canadian mineralogist, Special publication no. 3, Ottawa, Ontario, 494 p.

Duzgoren-Aydin, N. S., Aydin, A., and Malpas, J., 2002, Re-assessment of chemical weathering indices: Case study of pyroclastic rocks of Hong Kong: Eng. Geol., v. 63, p. 99–119.

Ehlen, J., 1999, Fracture characteristics in weathered granites: Geomorphology, v. 31, p. 29–45.

Ehlen, J., 2002, Some effects of weathering on joints in granitic rocks: Catena, v. 49, p. 91–109.

Geological Society Engineering Group Working Party Report, 1995, The description and classification of weathered rocks for engineering purposes: Q. J. Eng. Geol., v. 28, p. 207–243.

Gupta, A. S., and Rao, K. S., 2001, Weathering indices and their applicability for crystalline rocks: Bull. Eng. Geol. Env., v. 60, p. 201–221.

Heicht, C. A., 2000, Appolonian packing and fractal shape of grains improving geomechanical properties in engineering geology: Pure Appl. Geophys., v. 157, p. 487–504.

Kolibal, J., and Monde, J., 1998, Fractal image error analysis: Comput. Geosci., v. 24, p. 785–795.

Koptsik, G., Teveldal, S., Aamlid, D., and Venn, K., 1999, Calculations of weathering rate and soil solution chemistry for forest soils in the Norwegian–Russian border area with the PROFILE model: Appl. Geochem., v. 14, p. 173–185.

Krohn, C. E., 1988, Sandstone fractal and Euclidean pore volume distributions: J. Geophys. Res., v. 93, p. 3286–3296.

Lenton, T. M., 2001, The role of land plants, phosphorus weathering and fire in the rise and regulation of atmospheric oxygen: Global Change Biol., v. 7, p. 613–629.

Luca, D., Datcu, M., and Seidel, K., 1996, Multiresolution analysis of DEMs: Error and artifact characterization, *in* FRINGE'96: ESA Workshop on Applications of ERS SAR Interferometry, Zurich, Switzerland .

Mandelbrot, B., 1983, The fractal geometry of nature: W. H. Freeman, New York, 468 p.

Marcelino, V., Mussche, G., and Stoops, G., 1999, Surface morphology of quartz grains from tropical soils and its significance for assesing soil weathering: Eur. J. Soil Sci., v. 50, p. 1–8.

Marcelino, V., and Stoops, G., 1996, A weathering score for sandy soil materials based on the intensity of etching of quartz grains: Eur. J. Soil Sci., v. 47, p. 7–12.

Matsukura, Y., Hashizume, K., and Oguchi, C. T., 2002, Effect of microstructure and weathering on the strength anisotropy of porous rhyolite: Eng. Geol., v. 63, p. 39–47.

Meakin, P., 1993, The growth of rough surfaces and interfaces: Phys. Rep., v. 235, p. 189–289.

Meunier, J. D., Colin, F., and Alarcon, C., 1999, Biogenic silica storage in soils: Geology, v. 27, p. 835–838.

Moulton, K., and Berner, R., 1998, Quantification of the effect of plants on weathering: Studies in Iceland: Geology, v. 26, p. 895–898.

Oleschko, K., Parrot, J.-F., Korvin, G., Esteves, M., Vauclin, M., Ronquillo, G., and Brambila, F., 2004, Fractal image informatics: IEEE Trans. on Image Processing (Tip-01004-2004).

Orbach, R., 1986, Dynamics of fractal networks: Science, v. 231, p. 814–819.

Parrot, J. F., and Rico, J., 1997, Implementación y operación de un algoritmo para las mediciones fractales de las imágenes del suelo: Informe final, proyectos DGAPA: UNAM, Instituto de Geología, México, 35 p.

Pentland, A., 1984, Fractal-based description of natural scenes: IEEE Trans. Pattern Anal. Machine Intell., v. PAMI-6, p. 661–674.

Plotnick, R. E., Gardner, R., Hargrove, W. W., Prestegaard, K., and Perlmutter, M., 1996, Lacunarity analysis: A general technique for the analysis of spatial patterns: Phys. Rev. E, v. 53., p. 5461–5468.

Price, J. R., and Velbel, M. A., 2003, Chemical weathering indices applied to weathering profiles developed on heterogeneous felsic metamorphic parent rocks: Chem. Geol., v. 202, p. 397–416.

Radlinski, A. P., Radlinska, E. Z., Agamalian, M., Wignall, G. D., Lindner, P., and Randli, O. G., 1999, Fractal geometry of rocks: Phys. Rev. Lett., v. 82, p. 3078–3081.

Read, G., Kemp, R. A., and Rose, J., 1996, Development of a feldspar weathering index and its application to a buried soil chronosequence in southeastern England: Geoderma, v. 74, p. 267–280.

Rivas, T., Prieto, B., Silva, B., and Birginie, J. M., 2003, Weathering of granitic rocks by chlorides: Effect of the nature of the solution on weathering morphology: Earth Surf. Process Landforms, v. 28, p. 425–436.

Seffens, W., 1999, Order from chaos: Science, v. 285, p. 1228.

Smith, T. G., Lange, G. D., and Marks, W. B., 1996, Fractal methods and results in cellular morphology—dimensions, lacunarity and multifractals: J. Neurosci. Methods, v. 69, p. 123–136.

Strand, K., Passchier, S., and Näsi, J., 2003, Implications of quartz grain microtextures for onset Eocene/Oligocene glaciation in Prydz Bay, ODP Site 1166, Antarctica: PALAEO, v. 198, p. 101–111.

Stutter, M., Smart, R., and Cresser, M., 2002, Calibration of the sodium base cation dominance index of weathering for the River Dee catchment in north-east Scotland: Appl. Geochem., v. 17, p. 11–19.

Toennies, K. D., and Schnabel, J. A., 1994, Edge detection using local fractal dimension, computer-based medical systems, Proceedings of IEEE Seventh Symposium on Computer-Based Medical Systems: IEEE Computer Society Press, Winston-Salem, NC, p. 34–39.

Turner, M. J., Blackledge, J. M., and Andrews, P. R., 1998, Fractal geometry in digital imaging: Academic Press, Cambridge, UK, 328 p.

Voss, R. F., and Wyatt, J. C. Y., 1993, Multifractals and the local connected fractal dimension: Classification of early Chinese landscape paintings, *in* Crilly, A. J., Earnshaw, R. A., and Jones, H., eds., Applications of fractals and chaos: Springer-Verlag, New York, p. 171–184.

White, A. F., Blum, A. E., Schulz, M. S., Vivit, D. V., Stonestrom, D. A., Larsen, M., Murphy, S. F., and Eberl, D., 1998, Chemical weathering in a tropical watershed, Luquillo Montains, Puerto Rico: I. Long-term versus short-term weathering fluxes: Geochim. Cosmochim. Acta, v. 62, p. 209–226.

White, A. F., and Brantley, S. L., 2003, The effect of time on the weathering of silicate minerals: Why do weathering rates differ in the laboratory and field?: Chem. Geol., v. 202, p. 479–506.

Wong, T.-F., Fredrich, J., and Gwanmesia, G., 1989, Crack aperture statistics and pore space fractal geometry of Westerly granite and Rutland quartzite: Implications for an elastic contact model of rock compressibility: J. Geophys. Res., v. 94, p. 10267–10278.